ELSEVIER

Contents lists available at ScienceDirect

Journal of Non-Newtonian Fluid Mechanics

journal homepage: www.elsevier.com/locate/jnnfm



Viscoplastic surges down an incline

Y. Liu^{a,*}, N.J. Balmforth^a, S. Hormozi^b

- ^a Department of Mathematics, University of British Columbia, Vancouver, BC V6T 1Z2, Canada
- ^b Department of Mechanical Engineering, Ohio University, Athens, OH 45701-2979, USA



ABSTRACT

Asymptotic analyses and numerical computations are reported for surges of viscoplastic fluid down an incline with low inertia. The asymptotic theory applies for relatively shallow gravity currents. The computations use the volume-of-fluid method for tracking the interface; the constitutive law is dealt with by the augmented-Lagrangian method. The anatomy of the surge consists of an upstream region that converges to a uniform sheet flow, and over which a truly rigid plug sheaths the surge. The plug breaks further downstream due to the build up of the extensional stress acting upon it, leaving instead a weakly yielded superficial layer, or pseudo-plug. Finally, the surge ends in a steep flow front that lies beyond the validity of shallow asymptotics.

1. Introduction

Viscoplastic fluids are commonly encountered in natural settings in geophysics (e.g. mud and lava) and biology (mucus and blood clots), and feature in many engineering processes in, for example, the food (fruit pulp, dairy products and chocolate confections) and petroleum industries (drilling mud, cement and waxy crude oil). These materials flow like viscous fluid once stresses exceed a certain threshold (the yield stress), and remain solid-like otherwise. In fact, the most extensively used constitutive laws for these fluids (the Bingham and Herschel-Bulkley laws) discard any deformation below the yield stress, which complicates the modelling of viscoplastic flow from a mathematical perspective as it renders the stress state indeterminate and the effective viscosity singular at the yield point.

The spreading of viscoplastic fluid over an inclined surface has been studied experimentally in a number of previous studies, often with the goal of inferring the yield stress from steady flows [1–3] or the shape of a final deposit [4–7]. The most thorough and recent laboratory studies include the transient dam-break-type experiments of Ancey and coworkers [8–10] and a series of investigations on steady viscoplastic surges on inclined conveyor belts [11–13].

Theoretically, a model for shallow viscoplastic flow based on Reynolds lubrication theory has been widely used to complement such laboratory studies [14–16]. In this model, the long, thin flow is composed of a fully sheared region adjacent to the underlying surface buffered from the free surface by a plug-like zone. Importantly, that zone is not truly rigid, but deforms weakly in the direction of flow and is plug-like in that the transverse velocity profile is largely independent of depth. This structure is common in many shallow viscoplastic flows [17,18] and results from the separation of length scales in the directions aligned or perpendicular to flow. The border between the fully yield region and the plug-like zone is therefore not a true yield surface;

instead, it is often referred to as a fake yield surface, and the overlying zone as a pseudo-plug. Despite the fact that lubrication theory predicts the appearance of pseudo-plugs in shallow flows, it is also known that genuine rigid plugs can appear within these zones surrounding points of symmetry [17,19] or replace them in flow down almost uniform channels [20]. This raises the question of whether the superficial regions of a free-surface flow can also plug up in the far upstream extent of a steady surge flow, where the flow becomes almost uniform, as discussed in a qualitative way by Piau [21]. Indeed, for a truly steady surge that extends infinitely far upstream, one expects that the flow converges to a uniform sheat flow which, for a yield-stress fluid, is sheathed by a true plug

The purpose of the present study is to explore models for steady, shallow viscoplastic surges with a length that is sufficiently long that the flow converges to a steady sheet flow well upstream of the flow front; *i.e.* the theoretical analogue of the experiments by Chambon et al. [11–13]. For this task, we reconsider the lubrication analysis of Liu and Mei [14]. First, we consider the upstream extent of the surge to examine how the surge converges to uniform sheet flow, and how the corresponding superficial plug breaks as one progresses downstream. This demands a variation of the lubrication analysis that is designed for almost uniform flows, and parallels theory for flow down weakly varying channels [20]. Second, once the upstream plugged flow gives way to a fully yielded surge with a pseudo-plug, standard lubrication theory applies; for this region, we improve that theory by continuing the analysis to higher order in order to account better for non-shallow effects.

We complement the shallow-flow analysis with computations using the Volume-of-Fluid (VOF) method and an augmented Lagrangian scheme to deal with the yield stress. Such a combination of shallow-flow analysis and computation has proven effective in our previous work studying dambreak flows and their final shapes [22,23]. Here, we examine the extent to which the theoretical solutions match the observations

E-mail address: yliu0218@math.ubc.ca (Y. Liu).

^{*} Corresponding author.

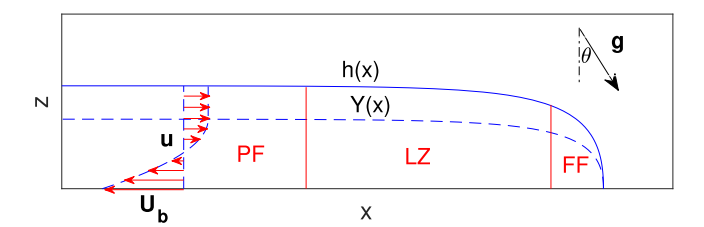


Fig. 1. Sketch of the geometry of the surge in the frame of reference in which there is no net flux and the flow is steady. The free surface is located at z=h; the level z=Y divides a fully yield region underneath from either a true plug or a weakly yielded pseudo-plug. The flow divides into three regions: a plugged flow region (PF) where the superficial layer of fluid is not yielded, a lubrication zone (LZ) where the pseudo-plug arises, and the flow front (FF) where the dynamics is not shallow.

of Chambon et al. and determine the conditions for which the pseudoplug of lubrication theory locks up into a true plug.

2. Formulation

2.1. Model equations

As sketched in Fig. 1, we consider a two-dimensional surge of incompressible viscoplastic fluid flowing steadily down a plane that is inclined at an angle θ to the horizontal. We use Cartesian coordinates aligned with the plane to describe the geometry; in the frame of reference of the surge, the inclined plane travels upslope with a speed u_b . We model the rheology of the fluid using the Herschel–Bulkley constitutive law. The governing equations for the velocity u=(u,w), deviatoric stress tensor τ , and pressure p are then

$$\nabla \cdot \boldsymbol{u} = 0,$$

$$\rho \left[\frac{\partial \mathbf{u}}{\partial t} + (\mathbf{u} \cdot \nabla) \mathbf{u} \right] = -\nabla p + \nabla \cdot \tau + \rho g \begin{pmatrix} \sin \theta \\ -\cos \theta \end{pmatrix}, \tag{1}$$

and

$$\begin{cases} \dot{\gamma}_{jk} = 0, & \tau_I < \tau_Y, \\ \tau_{jk} = \left(\kappa \dot{\gamma}^{n-1} + \frac{\tau_Y}{\dot{\gamma}}\right) \dot{\gamma}_{jk}, & \tau_I > \tau_Y, \end{cases}$$
 (2)

where ρ is the density, g is gravity, τ_Y is the yield stress, the plastic viscosity $\mu = \kappa \dot{\gamma}^{n-1}$ introduces the consistency κ and power-law index n as two further rheological parameters, and $\tau_I = \sqrt{\frac{1}{2} \sum_{j,k} \tau_{jk}^2}$ and $\dot{\gamma} = \sqrt{\frac{1}{2} \sum_{j,k} \dot{\gamma}_{jk}^2}$ denote second tensorial invariants, with

$$\dot{\gamma} = \begin{pmatrix} 2u_x & u_z + w_x \\ u_z + w_x & 2w_z \end{pmatrix}. \tag{3}$$

Here, subscripts on the velocity components represent partial derivatives

For the boundary conditions, we assume that there is no slip over the inclined plane, $u(x, 0) = (-u_b, 0)$, and that the upper surface is stress free, so that

$$\frac{\partial h}{\partial t} + u \frac{\partial h}{\partial x} = w$$
 and $(\tau - p\mathbf{I}) \cdot \begin{pmatrix} -h_x \\ 1 \end{pmatrix} = \begin{pmatrix} 0 \\ 0 \end{pmatrix}$, (4)

on z = h(x, t). The surge ends at a flow front, x = X(t), where $h \to 0$, and extends back upstream to where the flow converges to a uniform sheet flow.

2.2. The sheet-flow solution

In the frame of reference in which the net flux vanishes, the steady, uniform, sheet-flow solution is given by

$$(p, \tau_{xz}) = (1, \tan \theta) \left(1 - \frac{z}{H} \right) \rho g \cos \theta \tag{5}$$

and

$$u = u_{sheet}(z) = \frac{nU \tan^{1/n} \theta}{n+1} \times \begin{cases} \left[\frac{n}{2n+1} Y_{\infty}^{2+1/n} - (Y_{\infty} - \frac{z}{H})^{1+1/n} \right], & 0 < \frac{z}{H} < Y_{\infty}, \\ \frac{n}{2n+1} Y_{\infty}^{2+1/n}, & Y_{\infty} < \frac{z}{H} < 1, \end{cases}$$
(6)

where H is the flow depth and

$$U = \left(\frac{\rho g H \cos \theta}{\kappa}\right)^{1/n} H. \tag{7}$$

The level $z=HY_{\infty}$ corresponds to the yield surface above which the fluid is plugged, with

$$Y_{\infty} = 1 - \frac{\tau_Y}{\rho g H \sin \theta}.$$
 (8)

Note that, because there is no net flux along the plane in the frame of the surge, the profile in (6) demands that the speed of the inclined plane is

$$u_b = \frac{nV \tan^{1/n} \theta}{n+1} Y_{\infty}^{1+1/n} \left(1 - \frac{nY_{\infty}}{2n+1} \right). \tag{9}$$

The scales here can be used to non-dimensionalize the problem, as discussed later.

2.3. Volume-of-fluid computations

In our computations of the full problem, we use the VOF method to track the fluid interface using an advected volume fraction c(x, z, t) (see [22,23]). This scheme immerses the viscoplastic fluid beneath a miscible ambient Newtonian fluid. The material properties of the bulk mixture are set by linearly interpolating between the two phases using c, with the density and viscosity of the Newtonian fluid taken to be relatively small in order to minimize the effect of the ambient flow dynamics (cf. [22,23]).

To solve the governing equations, we evolve the system as an initial-value problem until a steady state is reached. We use an augmented-Lagrangian scheme to deal with the yield stress within a weak formulation of the problem [24,25], as implemented in C++ using the PELICANS platform (e.g. [26]). We refer the reader to our earlier work [22,23]) for further computational details, including a discussion of how we avoid any resolution issues stemming from the no-slip condition imposed on the underlying plane. Some additional details relevant for the present computations (including a resolution study confirming the fidelity of the computations) are provided in Appendix A.

The computational domain is finite, extending up to a height L_z and to a length L_x . The top and right-hand boundaries are chosen to be sufficiently distant that their positions do not affect the solution; free slip conditions are imposed to help suppress the ambient fluid dynamics. On the lower boundary we impose the fixed velocity $(u,w)=(-u_b,0)$, where u_b is chosen in a range that the flow adapts to reach a steady flow regime; for a long thin flow, the upstream current converges to the sheet flow solution above, and so u_b is given by (9).

To minimize the influence of the left-hand boundary conditions and ensure that the surge is mostly long and thin, we select domain lengths L_x that are as large as possible. To gauge the residual effect of the left-hand boundary conditions, we compute solutions with two different conditions: an infinitely long flow can be simulated by imposing the velocity here as that given by the sheet-flow solution; i.e. $(u,w)=(u_{sheet},0)$ at x=0. Alternatively, the back wall of the conveyor-belt experiment of [11–13] can be simulated by setting u=w=0 at x=0. Appendix A.3 summarizes the role played by these boundary conditions.

From c(x, z, t), we define the instantaneous position of the interface of the slump from the contour $c(x, z = h) = \frac{1}{2}$. The surface z = h(x) plays a major role in the asymptotic analysis of Section 3.

For the computations with Bingham fluid that we compare with asymptotic theory, we select parameters to minimize inertial effects

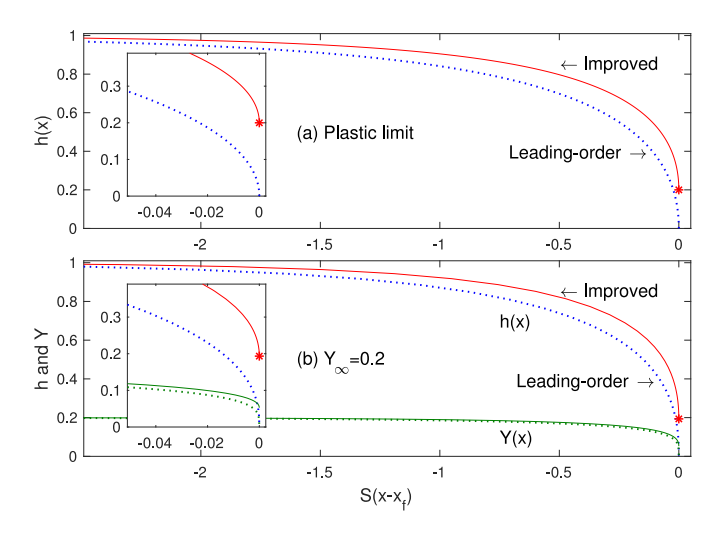


Fig. 2. Asymptotic surge solutions for (a) the plastic limit $Y \to 0$, and (b) $Y_{\infty} = 1 - S^{-1}B = 0.2$. The solid lines show the improved lubrication solutions for h(x) plotted against $S(x - x_f)$ with $\frac{1}{2}\epsilon\pi B = 0.2$ (as given by either Eqs. (41) and (42)); the dotted lines indicate the predictions of the leading-order theory. In (b), the corresponding fake yield surfaces Y(x) are also plotted. The insets show magnifications near the flow front.

(see Section 4.1 and Appendix A.2). The Herschel–Bulkley simulations of Section 4.2 have parameter settings matched to corresponding laboratory experiments; inertia may play a more significant role in these examples.

3. Asymptotic analysis

The anatomy of the surge is illustrated in Fig. 1: the flow body is divided into three regions. A plugged flow (PF) region arises at the back, where the surge converges to the sheet flow and a true plug exist on top of the fluid. That plug then breaks to leave a fully yielded flow with a more significant variation in the free surface. Although there is no true plug, the flow remains relatively shallow; in this lubrication zone (LZ), standard shallow-layer analysis applies and there is a superficial pseudo-plug. Finally, at the flow front (FF), the free surface steepens up to terminate the surge and invalidate shallow-layer theory.

To prepare the way for asymptotics, we rescale the equations to suit the shallow geometry [16]. We also focus on the special case of the Bingham model, with $\kappa \equiv \mu$ and n=1 (the extension to Herschel–Bulkley model is straightforward and partly described in Appendix B), and discard inertia. Hence, we introduce a characteristic depth H and horizontal length L with $\epsilon = H/L \ll 1$, and then set

$$z = H\hat{z}, \quad x = L\hat{x}, \quad u = U\hat{u}, \quad w = \epsilon U\hat{w},$$

$$p = \rho g H\hat{p}\cos\theta, \quad \tau = \rho g H\epsilon\cos\theta \begin{pmatrix} \sigma & \tau \\ \tau & -\sigma \end{pmatrix},$$

$$U = \frac{\rho g H^3\cos\theta}{\kappa L}, \quad S = \frac{\tan\theta}{\epsilon}, \quad B = \frac{\tau_Y L}{\rho g H^2\cos\theta}.$$
(10)

Notice that $S \sim \tan \theta$ is assumed here. For steady flow, the dimensionless equations now become, after dropping the hat decoration,

$$\begin{split} p_{x} &= \epsilon \sigma_{x} + \tau_{z} + S, \\ p_{z} &= \epsilon^{2} \tau_{x} - \epsilon \sigma_{z} - 1, \\ \tau &= \left(1 + \frac{B}{\dot{\gamma}}\right) \dot{\gamma}, \quad \sqrt{\tau^{2} + \sigma^{2}} > B, \\ 0 &= \int_{0}^{h} u(x, z) \, \mathrm{d}z, \\ \dot{\gamma}_{xx} &= 2\epsilon u_{x}, \quad \dot{\gamma}_{xz} = u_{z} + \epsilon^{2} w_{x}, \quad \dot{\gamma} = \sqrt{\dot{\gamma}_{xx}^{2} + \dot{\gamma}_{xz}^{2}}, \end{split} \tag{11}$$

with $u(x,0) = -u_h$ and

3.1. Plugged flow

In the PF region, the flow is nearly uniform, so we introduce the asymptotic sequences,

$$h = 1 + \epsilon h_1 + \dots, \quad p = 1 - z + \epsilon p_1 + \dots, \tag{13}$$

$$\tau = S(1-z) + \epsilon \tau_1 + \dots, \quad u = u_0 + \epsilon u_1 + \dots \tag{14}$$

and $\sigma = \sigma_0 + \dots$ The leading-order terms from (11) recover the velocity profile of the sheet-flow solution, this time in dimensionless form:

$$u_0 = -u_b + \frac{1}{2}S \times \begin{cases} z(2Y_{\infty} - z), & 0 < z < Y_{\infty}, \\ Y_{\infty}^2, & Y_{\infty} < z < 1, \end{cases}$$
 (15)

with

$$u_b = \frac{1}{6}SY_{\infty}^2(3 - Y_{\infty}) \tag{16}$$

and $Y_{\infty} \equiv 1 - \frac{B}{S}$. At $O(\epsilon)$ we now obtain

$$p_{1x}=\tau_{1z}+\sigma_{0x},$$

$$p_{1y} = -\sigma_{0z},\tag{17}$$

Expanding the free surface conditions about z = 1, we find

$$p_1 + \sigma_0 = h_1,$$

 $\tau_1 = Sh_1,$ at $z = 1.$ (18)

Hence, $p_1 + \sigma_0 = h_1$ throughout the fluid depth.

Over the fully yielded region underneath the plug, the constitutive law implies that

$$\sigma_0 = 0 \qquad \text{and} \qquad \tau_1 = u_{1z}. \tag{19}$$

It follows that $p_1 = h_1$ over this region, and so

$$\tau_1 = h_{1x}z + T$$
 and $u_1 = \frac{1}{2}h_{1x}z^2 + Tz$, (20)

where T(x) is not yet determined. However, in the overlying plug, σ_0 cannot be taken to vanish and the stress state is indeterminate, as (17) do not determine all of p_1 , τ_1 and σ_0 . Instead, the yield condition demands only that $\sigma_0^2 < B^2 - S^2(1-z)^2$.

The stress solution for the yielded region,

$$\tau \sim S(1-z) + \epsilon(h_{1x}z + T)$$
 and $\sigma = O(\epsilon)$, (21)

now implies that the yield surface is shifted to $Y = Y_{\infty} + \epsilon Y_1$, where

$$Y_1 = S^{-1}(h_{1x}Y_{\infty} + T). (22)$$

However, the plug speed must remain equal to $\frac{1}{2}SY_{\infty}^2$ as there is no deformation in h>z>Y. This demands that $u_1(x,Y)=0$, or

$$T = -\frac{1}{2}Y_{\infty}h_{1x}. (23)$$

Finally, we impose the flux constraint,

$$\int_0^h u \, \mathrm{d}z = 0 \tag{24}$$

which gives, at $O(\epsilon)$,

$$u_b h_1 = \frac{1}{2} S Y_{\infty}^2 h_1 + \frac{1}{6} h_{1x} Y_{\infty}^3 + \frac{1}{2} T Y_{\infty}^2. \tag{25}$$

Hence,

$$h_{1x} = 2Sh_1$$
 and $Y_1 = Y_{\infty}h_1$, (26)

and so the departure from the uniform sheet solution grows exponentially in the downslope direction, with an exponent given by 2S.

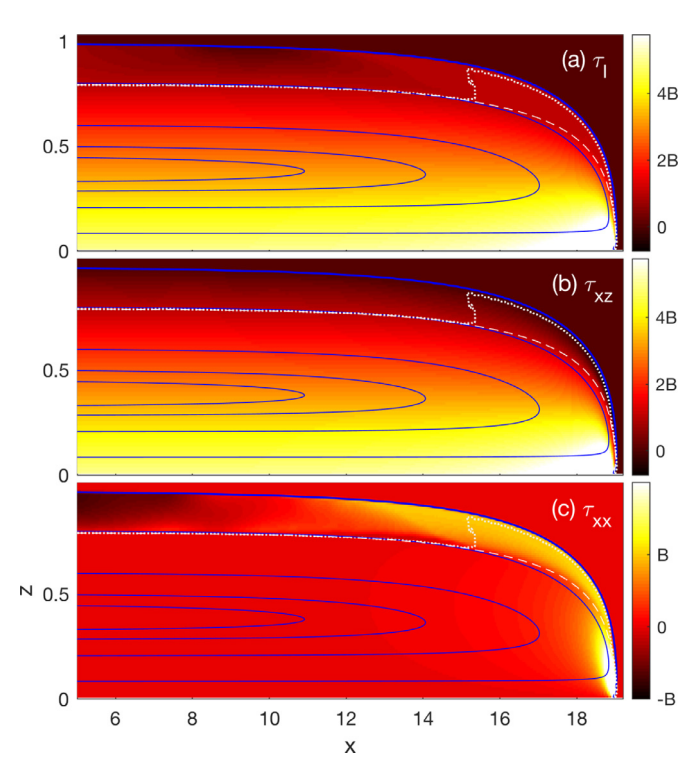


Fig. 3. Numerical solution for $\theta=10^\circ$ and $Y_\infty=0.8$ showing (a) τ_I , (b) τ_{xz} and (c) τ_{xx} . The darker (blue) lines show sample streamlines and the dotted white line is the true yield surface where $\tau_I=B$. The dashed line shows the contour level where $\tau_{xz}=B$. (For interpretation of the references to colour in this figure legend, the reader is referred to the web version of this article.)

3.2. Breaking the plug

Returning to (17), we now observe that, over the plug,

$$h_{1x} = 2\sigma_{0x} + \tau_{1z},\tag{27}$$

which can be integrated from $z = Y_{\infty}$ upto z = 1 to give

$$\frac{\partial}{\partial x} \int_{Y_{\infty}}^{1} \sigma_0 \, \mathrm{d}z = \frac{1}{2} S h_1 (1 - Y_{\infty}). \tag{28}$$

Hence

$$\int_{Y_{\infty}}^{1} [\sigma_0(x, z)]_{-\infty}^x \frac{\mathrm{d}z}{1 - Y_{\infty}} = \frac{1}{4} h_1, \tag{29}$$

which, given that $|h_1|$ grows exponentially, implies that the net jump in extensional stress across the plug must also increase towards the flow front. Moreover, since h_1 must eventually become $O(\epsilon^{-1})$ to curve the surge, the plug must inevitably break.

A further constraint is provided by the unyielded condition of the plug (given the leading-order shear stress $\tau \sim S(1-z)$),

$$-\sqrt{B^2 - S^2(1-z)^2} < \sigma_0 < \sqrt{B^2 - S^2(1-z)^2},\tag{30}$$

which bounds the integral on the left of (29). In particular, that integral cannot exceed $\frac{1}{2}\pi B$ in absolute size. Therefore, the plug must have broken when

$$|h_1| > 2\pi B. \tag{31}$$

3.3. Lubrication zone

The preceding analysis indicates that the plug breaks when $h-1=O(\epsilon)$. Downstream, the departure from the sheet-flow solution grows

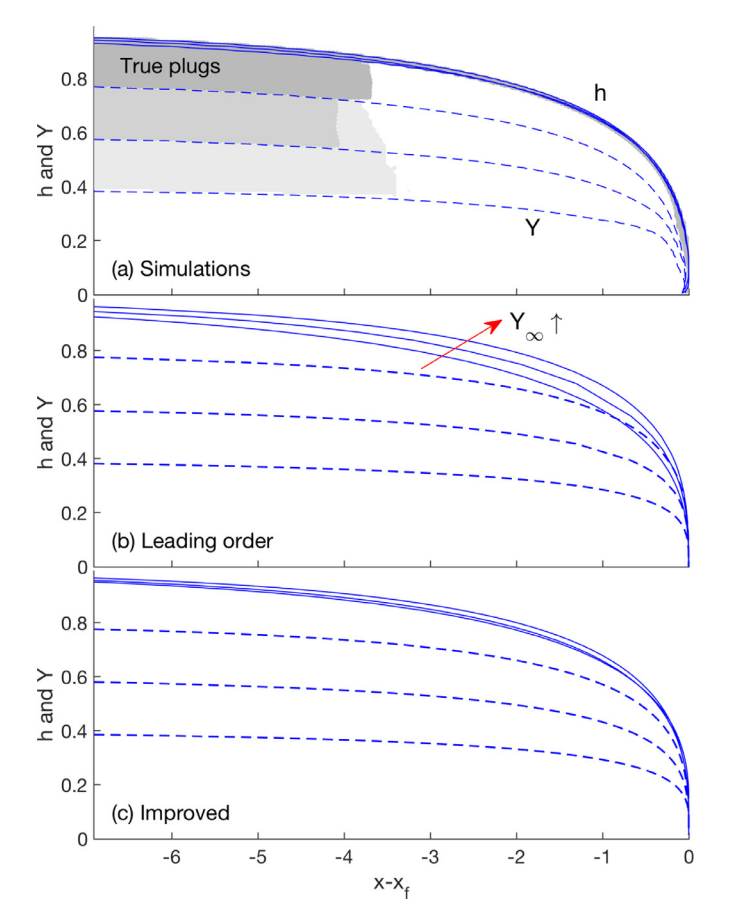


Fig. 4. Flow profiles and fake yield surfaces for (a) numerical simulations, (b) leading-order lubrication theory and (c) improved asymptotic theory (using (42)), with $\theta=10^\circ$ and $Y_\infty=0.4$, 0.6 and 0.8. The solid and dashed lines show h and Y, with Y defined as the contour level where $\tau_{xz}=B$ for the simulations. The flow profiles steepen with increasing Y_∞ . The shaded regions in (a) show the true plugs (which extend up to the free surface in each case, and with the shading darkening with increasing Y_∞).

further as we enter the lubrication zone and h-1 becomes O(1). With $h=h(x)\neq 1$, the leading-order solution of (11) now furnishes the standard lubrication result for the velocity profile,

$$u \sim -u_b + \frac{1}{2}(S - h_x) \times \begin{cases} z(2Y - z), & 0 < z < Y, \\ Y^2, & Y < z < h, \end{cases}$$
 (32)

where Y = Y(x) is the position of the fake yield surface. The profile of the surge itself follows from solving

$$Y = h - \frac{B}{S - h_x},$$

$$u_b h = u_p \left(h - \frac{1}{3} Y \right)$$

$$(33)$$

where

$$u_p = \frac{1}{2}(S - h_x)Y^2 \tag{34}$$

determines the speed of the overlying pseudo-plug. Over that region, the extensional stress is given by

$$\sigma = \operatorname{sgn}(u_{px}) \sqrt{B^2 - (S - h_x)^2 (h - z)^2}, \tag{35}$$

which matches one of the limits in (30) for $h \to 1 + O(\epsilon)$. Thus, the plugged flow is expected to match continuously to the lubrication zone once the plug breaks.

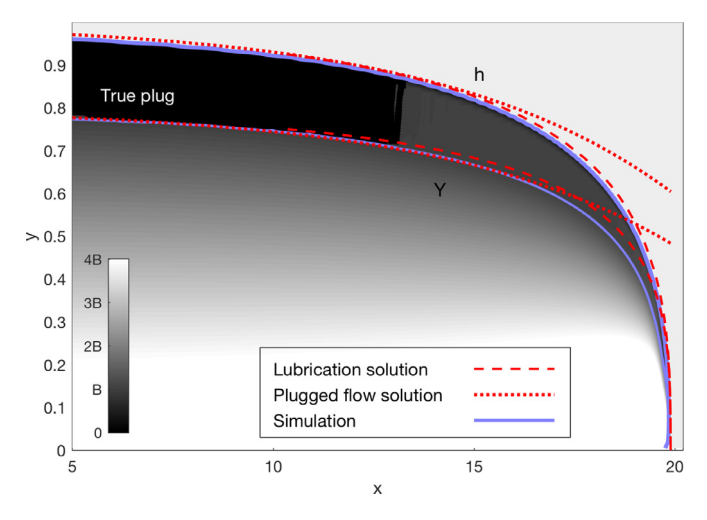


Fig. 5. Numerical solution for $Y_{\infty} = 0.8$ and $\theta = 5^{\circ}$ (B = 0.0175), showing a density plot of τ_I with z = h(x) and the fake yield surface superposed; the true plug is shaded black. The dashed lines show the prediction of the leading-order lubrication theory (with the flow front aligned). The dotted lines show the predictions of the plugged-flow solution in (26), with 1 - h matched to the simulation at x = 5.

Note that (33) predicts that h and Y converge exponentially to the sheet flow solution as $x \to -\infty$. In particular,

$$h_x \sim \frac{1}{2}S(h-1)\frac{Y_{\infty}^2 - 3Y_{\infty} + 6}{Y_{\infty}^2 - 3Y_{\infty} + 3},$$

$$Y - Y_{\infty} \sim \frac{1}{2}Y_{\infty}(h-1)\frac{Y_{\infty}^2 - 2Y_{\infty} + 3}{Y_{\infty}^2 - 3Y_{\infty} + 3}.$$
(36)

Because $0 < Y_{\infty} < 1$, this result implies that the fake yield surface lies above the true yield surface once we enter the plugged flow region where $h-1=O(\epsilon)$. Thus, one does not expect a pseudo-plug to intervene between the fully yielded zone and the true plug (cf. [20]).

3.4. Improving the lubrication theory

With a little effort, as described in Appendix B, the lubrication theory can be continued to next order to furnish the improved model,

$$Y = h - \frac{B}{S - h_x} + \frac{1}{2} \epsilon \pi B^2 \frac{h_{xx}}{(S - h_x)^3},$$

$$u_b h = u_p \left(h - \frac{1}{3} Y \right) + \frac{1}{2} \epsilon \pi B^2 \frac{u_{px}}{(S - h_x)^2},$$
(37)

in place of (33). In principle, this improved model better captures non-shallow effects. In the limit of $\theta=0$ and $u_b=0$, the system in (37) reduces to the problem for a collapsed two-dimensional slump [22]. In the limit $u_b=0$, the time dependence can be retained to furnish an improved lubrication model for unsteady viscoplastic flow over an inclined surface.

The plastic limit of (37) is achieved when $Y \rightarrow 0$ throughout the surge, and permits further analytical headway in constructing the surface profile. Setting Y = 0 in the first equation in (37) furnishes

$$h - \frac{B}{S - h_x} + \frac{1}{2} \epsilon \pi B^2 \frac{h_{xx}}{(S - h_x)^3} = 0.$$
 (38)

Given that $Y \to 0$ demands that $B/S \to 1$ at the back of the surge, the leading-order solution is

$$h + \log(1 - h) \sim S(x - x_f),$$
 (39)

which corresponds to the final shape of an inclined dambreak [14,15]. Continuing with the improved model, (38) is equivalent to

$$(S - h_x)h - S + \frac{1}{2}\epsilon\pi Bh_x = O(\epsilon^2),\tag{40}$$

or

$$h - \frac{1}{2}\epsilon\pi B + \left(1 - \frac{1}{2}\epsilon\pi B\right)\log\left(\frac{1 - h}{1 - \frac{1}{2}\epsilon\pi B}\right) \sim S(x - x_f),\tag{41}$$

if $x=x_f$ denotes the front position. Note that the front of the surge here has finite height, with $h(x_f)=\frac{1}{2}\epsilon\pi B$, as found in [22]. Further discussion of the slumped shapes predicted by (38) and (41) is provided in Appendix C.

Away from the plastic limit, we can again iterate (37) to $O(\epsilon^2)$ into the second-order system,

$$\begin{split} B - (h - Y)(S - h_X) &= \frac{1}{2} \varepsilon \pi B(h_X - Y_X), \\ u_b h - u_p \left(h - \frac{1}{3} Y \right) &= \frac{1}{4} \varepsilon \pi B Y [(2h - Y)Y_X - Y h_X]. \end{split} \tag{42}$$

Beginning from a position upstream where the surge is close to the sheetflow solution, this system can be integrated downstream to the flow front using initial conditions based on (36). Again, the surge ends at finite depth where the free surface becomes vertical and h and Y are $O(\epsilon)$. A sample solution with $Y_{\infty}=0.2$ (B/S=0.8) is shown in Fig. 2 and compared with the predictions of the leading-order lubrication model and the corresponding solutions in the plastic limit.

4. Numerical results

4.1. Comparison with asymptotics

In this section, we report computations with the Bingham model, n=1, for comparison with the asymptotic analysis. Following along the lines of that theory, we also place the problem into a dimensionless form by scaling variables using the depth of the expected sheet flow H and its characteristic velocity \mathcal{U} . The stresses are scaled by $\rho gH\cos\theta$. In addition, in the computations, there is no significance to the lengthscale L, so we set L=H which is equivalent to taking $\epsilon=1$. Shallow surges then arise when the longitudinal length far exceeds the depth. We use Y_{∞} and θ as the main parameters, which translate to a dimensionless belt speed and yield stress of

$$\begin{cases} u_b = \frac{1}{6} Y_\infty^2 (3 - Y_\infty) \tan \theta \\ B = (1 - Y_\infty) \tan \theta \end{cases}$$
(43)

In all the computations we report in this subsection, inertia is not sufficient to significantly affect the solution (see Appendix A.2), and we use left-hand boundary conditions given by an upstream sheet-flow solution.

Fig. 3 shows a sample solution with $\theta=10^\circ$ and $Y_\infty=0.8$. The plots show the deviatoric stress invariant and components as densities over the (x,z)-plane. Superposed are streamlines and the free surface, with an upstream section of the solution not shown in order to remove the regions where the boundary conditions at x=0 play a role. The shear stress τ_{xz} matches the stress invariant τ_I throughout the lower part of the surge, but deviates over a superficial layer adjacent to the free surface. There, the Augmented Lagrangian algorithm detects a genuine plug¹ for $x\lesssim 15$. This plug then breaks to leave, over $15\lesssim x\lesssim 18$, a weakly yielded superficial region with $\tau_I\sim B$; i.e. a pseudo-plug. In the numerical simulations, the fake yield surface z=Y(x) can be picked out by determining the level where $\tau_{xy}=B$ (see Fig. 3). The true and fake yield surfaces are continuous at the breakage of the plug. All this anatomy of the surge was already anticipated by the asymptotic analysis in Section 3.

Fig. 4 shows sample flow profiles h(x) and fake yield surfaces Y(x), for $\theta = 10^{\circ}$ and varying Y_{∞} . The two panels compare the simulations

 $^{^1}$ Although the stress field is indeterminate here, the algorithm provides an admissible solution for the plug which is dictated by the iterative scheme. The borders of the true plug are a little rough due to grid-dependent numerical errors. However, the plugs appear to be robustly detected given that the stress invariant τ_I lies significantly below B over this part of the surge.

Table 1 Experimental parameters from [13].

	τ_{Y} (Pa)	κ (Pa s^n)	n	θ (°)	u_b (m/s)
C2	7.2	5.1	0.41	11.9	0.26
C5	7.2	5.0	0.43	15.3	0.148

with the predictions of the leading-order and improved asymptotic theories. The latter leads to a mildly better comparison of h(x), correcting for a spread in the predicted profiles which are found in the simulations to collapse closely to one another. However, the improved asymptotics theory does not lead to a substantially better agreement with the simulations in the examples shown in Fig. 4 because the lubrication zone in these solutions is not particularly long, with the free surface steepening up quickly from the plugged flow upstream to the flow front.

We provide a more quantitative comparison of a numerical solution for $Y_{\infty}=0.8$ and $\theta=5^{\circ}$ with the asymptotic theory in Fig. 5. This figure highlights the free surface, the true plug of the numerical solution, and the fake yield surface underneath the pseudo-plug (again defined by $\tau_{xz}=B$ in the simulations). These are compared with the predictions of the plugged flow solution (26) and the leading-order lubrication theory (Section 3.3). The plug breaks in the simulation when $1-h\approx0.12$, in satisfying agreement with the prediction $1-h=2\pi B=0.11$ of Section 3.2.

4.2. Comparison with experiments

Chambon et al. [11–13] have presented a comprehensive experimental study on viscoplastic surges on a conveyor belt. For comparison with their results, we perform numerical simulations matching some of their experimental parameters. More specifically, we choose the two sets of parameters denoted by C2 and C5 in [13]. The rheology of the two samples and the inclination and speed of the belt are given in Table 1. The fluid in these experiments is an aqueous suspension of Carbopol with density $\rho=10^3$ kg/m³. We employ a no-slip back wall to provide the left-hand boundary conditions.

Figs. 6-8 display the results of the computations. Fig. 6 plots the velocity field for experiment C5, and corresponds to Fig. 6 in [13]. Figs. 7 and 8 show the strain-rate field, surface velocity and sample vertical profiles of the velocity components in the frame of the conveyor belt for both experiments (for comparison with their Figs. 9 and 10). Distances are scaled by the thickness of the expected uniform sheetflow, H, and velocities by the mean downslope velocity \overline{u} (the scalings used by Chambon et al.). Although the identification of the true plug is more difficult (owing to the power-law viscosity of the Herschel-Bulkley law), the computations still detect that the stress invariant near the free surface falls below the yield stress a scaled distance of about four units behind the flow front for C2, and three units for C5. The figures also contrast the numerical results with the predictions of the leading-order lubrication theory, which performs well in reproducing the simulations. Evidently, the fine details of the plugged flow or the improved lubrication theory are minor, and non-shallow flow effects are insignificant away from the flow front. Importantly, the numerical solutions converge towards the uniform-flow state at the back of the surge (over a longitudinal distance of about 10H; see Appendix A.3), and there is no mismatch between H and the depth at the back of the surge. This supports the inference of Chambon et al. that some rheological effect is responsible for their observation that the experimental surges are deeper than the expected sheet flow.

The broad match between simulations and leading-order lubrication is somewhat better than Chambon et al.'s comparison of experiments and asymptotics, although there is qualitative agreement between all three. For example, the differences between the predictions of lubrication theory and simulations for the surge profile and surface velocity are very small in Figs. 7 and 8, unlike the corresponding figures of

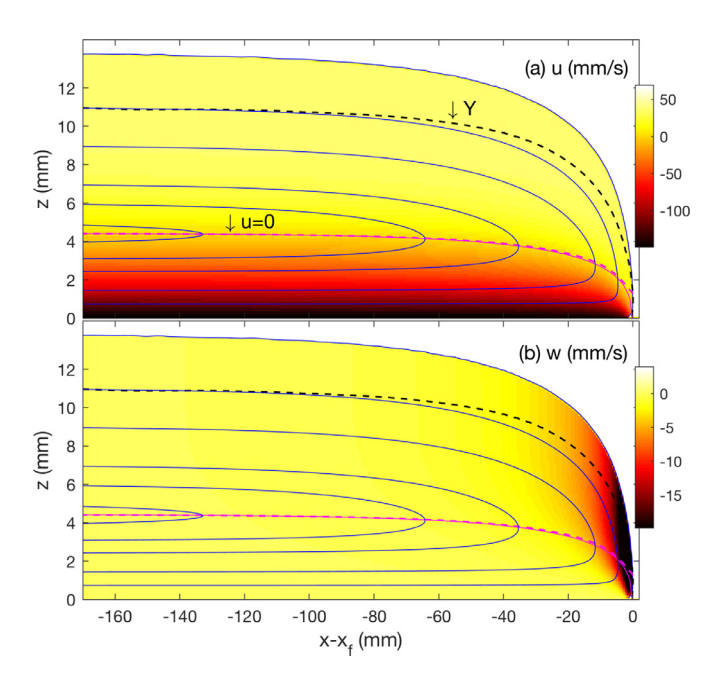


Fig. 6. Experiment C5 of [13], showing (a) u(x, z) and (b) w(x, z) as densities over the (x, z)-plane, for a qualitative comparison with their Fig. 6. A selection of streamlines is also shown (thinner blue lines). The dashed lines shows the levels where u = 0 and z = Y ($\tau_{xz} = B$). In leading-order lubrication theory, u = 0 along $z = Y - Y[nY/h(2n+1)]^{n/(n+1)}$; this prediction is also drawn as the lighter (pink) solid line. (For interpretation of the references to colour in this figure legend, the reader is referred to the web version of this article.)

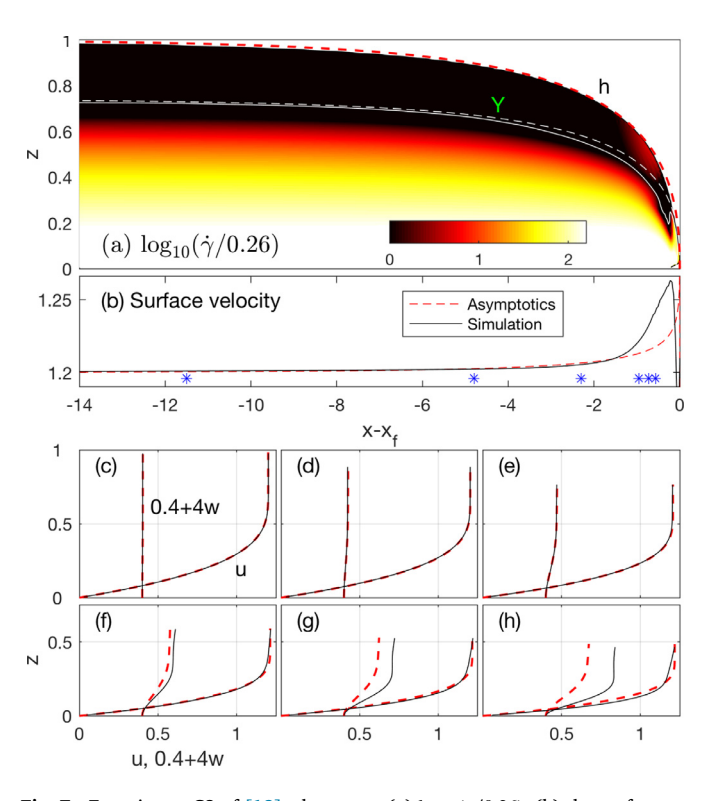


Fig. 7. Experiment C2 of [13]: shown are (a) $\log_{10}(\dot{\gamma}/0.26)$, (b) the surface velocity, and (c)–(h) velocity profiles at the x–positions indicated in (b), for a comparison with figure 10 in [13] (the scaling factor of 0.26 being selected in that paper). The (red) dashed lines indicate the predictions of the leading-order lubrication theory. In (a) the solid white line shows the contour $\tau_{xz} = B$, whereas the dashed white line is the fake yield surface z = Y(x) of the leading-order lubrication theory. (For interpretation of the references to colour in this figure legend, the reader is referred to the web version of this article.)

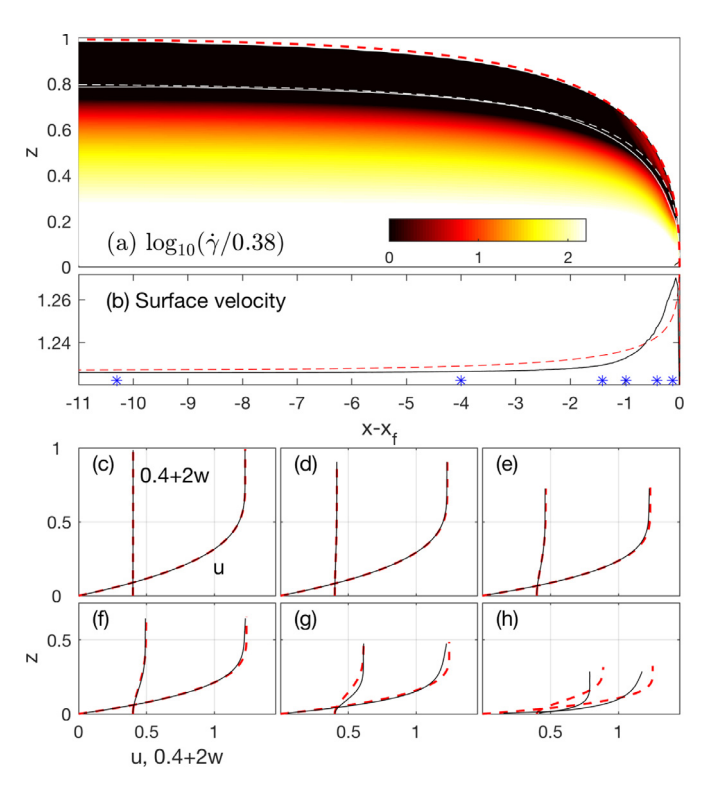


Fig. 8. A similar picture to Fig. 7, but for Experiment C5 of [13] and for comparison with their Fig. 9 (with $\log_{10}(\dot{\gamma}/0.38)$ plotted in (a), as in that paper).

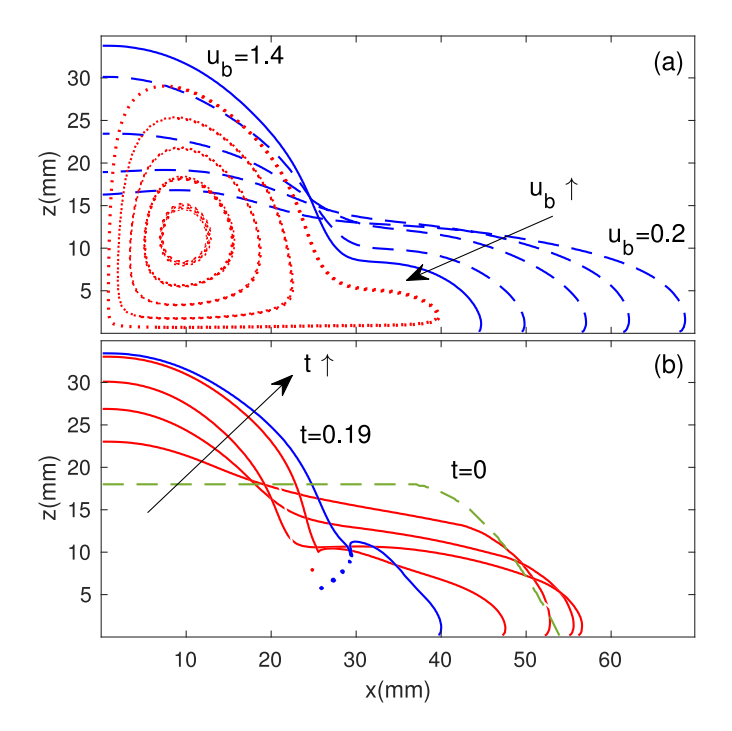


Fig. 9. Flow profiles for a simulation with $\theta=14.6^\circ$, $\tau_Y=6$ Pa, $\kappa=6.65$ Pa s^n and n=0.405 (the experiment C_PIV of [12]), for (a) $u_b=0.2$, 0.4, 0.8, 1.2 and 1.4 m/s, in the steady state, and (b) $u_b=1.6$ m/s at a succession of times, starting from the initial profile shown by the dashed line (t=0, 0.06, 0.08, 0.11, 0.17 and 0.19 s). In (a), the profile for $u_b=1.4$ m/s is shown by the solid line and several streamlines are also plotted (dotted lines).

[13], which reveal noticeable differences. The front of the experimental surges are also rounded and overturn, as in the simulations but not the asymptotics, although the nose occurs at dimensionless heights of about 0.25-0.3 whereas it lies well below 0.1 in the simulations. We interpret all this to imply that the shallow approximation is not responsible for the main quantitative disagreements between theory and experiment.

We quantify this further using two distance diagnostics defined by Chambon et al. The first of these records the distance from the flow front, $x_{fc,u} = |x - x_f|$, where

$$\left[\int_0^h (u_{exp} - u_{asy})^2 \, \frac{\mathrm{d}z}{h} \right]^{1/2} = 0.07\overline{u}$$

where the subscripts refer to PIV measurements and the leading-order asymptotic prediction, and \overline{u} is again the mean donwslope speed. Chambon et al. quote values for $x_{fc,u}$ from 0.5H to H for all their experiments. The same mean difference between the velocity profiles of our simulations and the asymptotics indicates that $x_{fc,u} \approx 0.34H$ for C2 and 0.18H for C5. In other words, the asymptotic prediction for the velocity profile remains close to that of the simulation for distances much nearer the flow front.

The second diagnostic denotes the distance, $x_{fc,h} = |x - x_f|$, from the flow front where $|h_{sim} - h_{asy}|$ reaches 0.6 mm. Again, Chambon et al. find that $x_{fc,h}$ is order of H; this time, they quote values between 1.5H and 2H for their tests. By contrast, in our C2 simulation, $x_{fc,h} = |h_{sim} - h_{asy}| \approx 0.3 H$, whereas the difference in flow depths never reaches such a threshold for C5, always being less than 0.3 mm.

All the experimental or asymptotic results described above relate to relatively shallow surges. As the belt speed increases, however, the surge shortens and deepens, leading to profiles like those shown in Fig. 9(a). In these cases, the aspect ratio of the flow profile is O(1), with the fluid beginning to climb up the (no-slip) back wall. Raising the belt speed still further leads to a sudden catastrophic overturning event that interrupts the passage to a steady equilibrium, as illustrated in Fig. 9(b). In this case, the fluid climbs up the wall before collapsing down in the manner of a breaking wave; bubbles of ambient fluid become entrained into the surge and the reliability of the simulation is quickly lost, leading us to terminate the computation before any convergence to a steady state. At this stage it is not clear whether the overturn heralds the loss of the steady state and the onset of a continued cascading flow. As far as we are aware, this type of dynamics has not yet been observed experimentally.

5. Concluding remarks

We have conducted a theoretical study of viscoplastic surges down an inclined surface, combining asymptotic analysis with numerical simulations. We have focussed on the steady states reached in frames moving at constant speed down the slope, although we have also reported a situation in which such steady surges do not appear to be attainable and an unsteady cascading state is reached instead. The numerical computations of shallow surges mostly agree with the asymptotic predictions, more so than the experiments by Chambon et al. [11–13], which are less comparable with the asymptotics though still in broad agreement. That discrepancy between the experiments and asymptotics is not therefore the result of non-shallow flow effects, but must originate elsewhere.

The computations confirm the phenomenology expected for a surge, namely that there is an upstream sheet flow with a rigid plug that breaks as one moves downstream due to the build up of the extensional stress across the plug. This leaves a weakly yield zone atop the fluid, the pseudo-plug, as predicted by standard lubrication theory. The surge eventually steepens and terminates at a relatively abrupt flow front.

We have chiefly operated in the limit in which inertial effects play little role in the surge, which is clearly a limitation with regard to many applications in the geosciences. In particular, we have not catalogued any secondary instabilities of the steady surges (such as roll waves [27]) or found any multiple equilibria, both of which might well appear at higher Reynolds number. We leave such considerations for future work.

Acknowledgements

S.H. acknowledges financial support by NSF (Grant No. CBET-1554044-CAREER).

Appendix A. Additional numerical details

In this appendix we provide further details of the numerical computations. We use the dimensionless version of the problem in which lengths are scaled by H and velocities by \mathcal{U} as in Section 4.1.

To find the steady surge states, we solve suites of initial-value problems in the frame of reference of the surge, following the strategy outlined in [22,23]. We begin from initial conditions in which motionless viscoplastic fluid is deposited on the inclined plane with a rectangular shape whose depth is set by the sheet-flow solution. The front of the rectangle is smoothed over a streamwise scale of order of a fraction of the fluid depth using a arc tangent function. The simulations do not appear to be sensitive to the initial condition, at least at the Reynolds numbers chosen for most of our simulations (Section A.2), with no indication of multiple equilibria or unsteady states (but see the discussion surrounding Fig. 9).

The initial-value problem is solved exploiting the PLIC (Piecewise Linear Interface Calculation) algorithm to evolve the interface within the volume-of-fluid scheme. The essential details of the algorithm can be found in [28], although we modify it slightly to surmount a numerical difficulty arising from an unresolved layer of the ambient fluid coating the inclined plane, as is described in [22,23]. In brief, the modification amounts to monitoring the volume fraction adjacent to the inclined plane and adjusting the value of c there if it exceeds a threshold (set to 0.99). This replacement of ambient fluid with yield-stress material destroys mass conservation, which is restored by rescaling the flow height uniformly over the length of the surge, incurring a further error, of order a fraction of a grid spacing.

The evolution observed in these initial-value problems suggest that the final steady states possess no contact line along the underlying plane. Rather, a continually thinning finger of ambient fluid coats the plane as one progresses upstream. Therefore, although the adjustment to the PLIC algorithm applies an approximation to allow the contact line of the initial condition to migrate with the plane to create this finger, once that feature is established, the scheme simply amounts to neglecting the small amount of ambient fluid within the finger once it becomes thinner than the lowest grid cell. This prevents interpolation errors in the velocity field and shear stress of the finger from excessively lubricating the surge, and permits the computation to otherwise remain resolved, as we now document.

A1. Resolution study

Fig. A.1 shows the results of a resolution study for the profile of a Bingham surge with $\theta=\pi/18$ and B=0.0522 (Re=1, $u_b=0.041$ and the total area of fluid is 24). At the rear of the surge, a no-slip back wall is imposed, and the grid spacing is uniform with $\Delta x=4\Delta z$. Varying that grid spacing by a factor of 8 (as indicated) furnishes barely any discernible difference in the free surface profile. Indeed, the root-mean-square difference in the velocity field, defined as

$$\sqrt{\frac{\iint |\boldsymbol{u} - \boldsymbol{u}_*|^2 c_* \, \mathrm{d}x \, \mathrm{d}y}{\iint c_* \, \mathrm{d}x \, \mathrm{d}y}},$$

between the coarsest and finest of these simulations is about $0.088u_b$, and decreases to $0.025u_b$ between the two finest simulations. Here, c_* and u_* denote the reference solution, which is that for the finest simulation, interpolated onto the grid of the coarser solution. Also shown are selected contours of constant shear stress τ_{xz} (which closely match those of τ_I below the plug), illustrating the convergence with resolu-

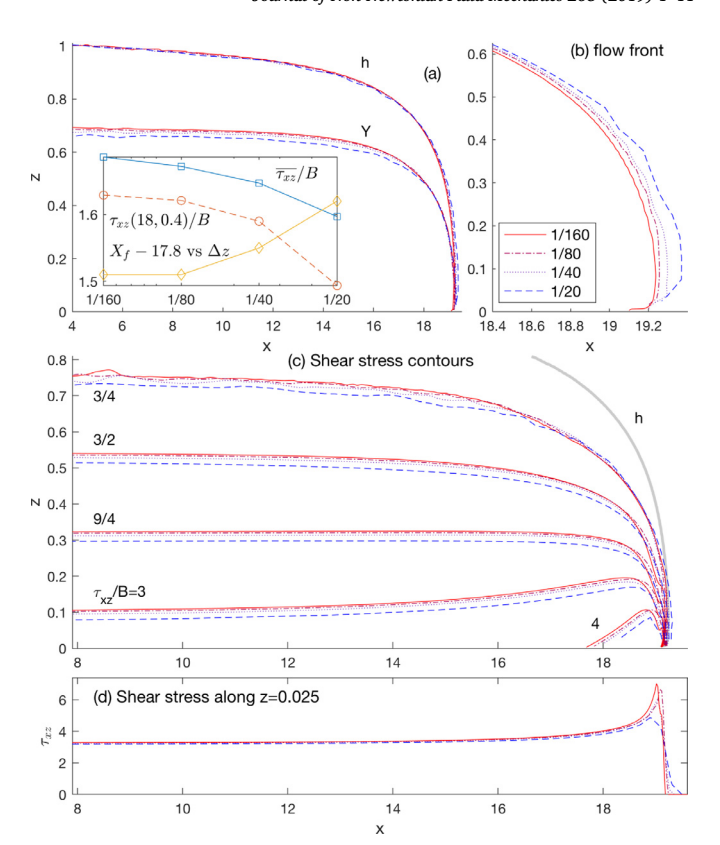


Fig. A.1. Simulations of a Bingham surge profile with $\theta=10^\circ$ and B=0.0522 ($Y_\infty=0.7$, fluid area of 24, $u_b=0.041$ and Re=1) with the grid sizes indicated. (a) shows h and Y; (b) a magnification near the flow front; (c) contours of constant τ_{xz}/B , as indicated (with the surge profile of the finest resolution case shown by the lighter grey line); (d) the shear stress along z=0.025 (the lowest grid cell of the coarsest computation). In (a), the inset shows the flow front X_f , mean shear stress, $\overline{\tau_{xz}}/B=\int\int(\tau_{xz}/B)\,c\,\mathrm{d}x\,\mathrm{d}z$, and τ_{xz} at the point (x,z)=(18,0.4), all plotted against the vertical grid spacing Δz ($\Delta x=4\Delta z$). The convergence of $\overline{\tau_{xz}}$ is impeded by the need to resolve the sharply localized region of high stress underneath the flow front (cf. Fig. 3 and panels (c) and (d)).

tion, at least for stress levels sufficiently in excess of B. Contours closer to B show significantly less degree of convergence, as highlighted by the roughness of the yield surfaces plotted in Fig. 4, and the stress solution remains sensitive to resolution for $\tau_I < B$. These latter deficiencies are not problematic as the solution is independent of the stress state over the plug as long as the fluid there is not yielded. Note that the computations reported in Section 4 and the remainder of this appendix all use the finest grid of the resolution study.

A2. Inertial effects

Fig. A.2 shows numerical simulations of Bingham surges with varying Reynolds number Re= HV/κ from 0.1 to 10 (which span the range of all the simulations reported in this study), with a back wall providing the left-hand boundary conditions. With the scalings of the problem outlined in Section 4.1, the dimensionless problem retains the Reynolds number only as a factor in front of the inertial terms. Consequently, the flow profile becomes independent of Re in the inertialess limit. Indeed, the flow profiles and stress levels shown in Fig. A.2 closely collapse (save for the relatively rough yield surface) and the root-mean-square differences in the velocity field and stress invariant are less than $4 \times 10^{-3} u_b$ and 0.01B, respectively. Thus we conclude that inertial effects are not significant. The computations reported in Section 4.1 are conducted with Re = 1.

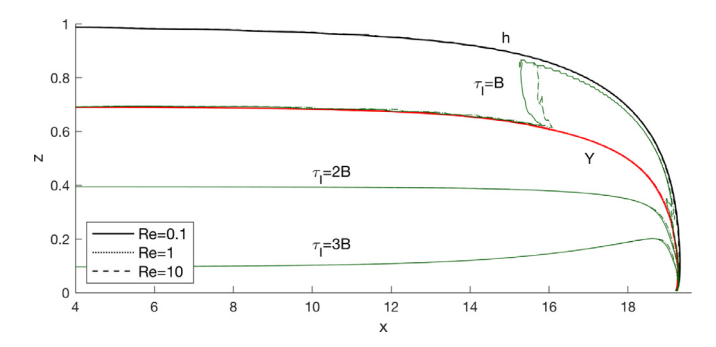


Fig. A.2. Simulations of Bingham surges for $\theta=10^\circ$, $u_b=0.041$ and B=0.0522 ($Y_\infty=0.7$) for the Reynolds numbers indicated (the total area of fluid is 24). Plotted are h, Y ($\tau_{xz}=B$) and the stress levels $\tau_I/B=1$, 2 and 3.

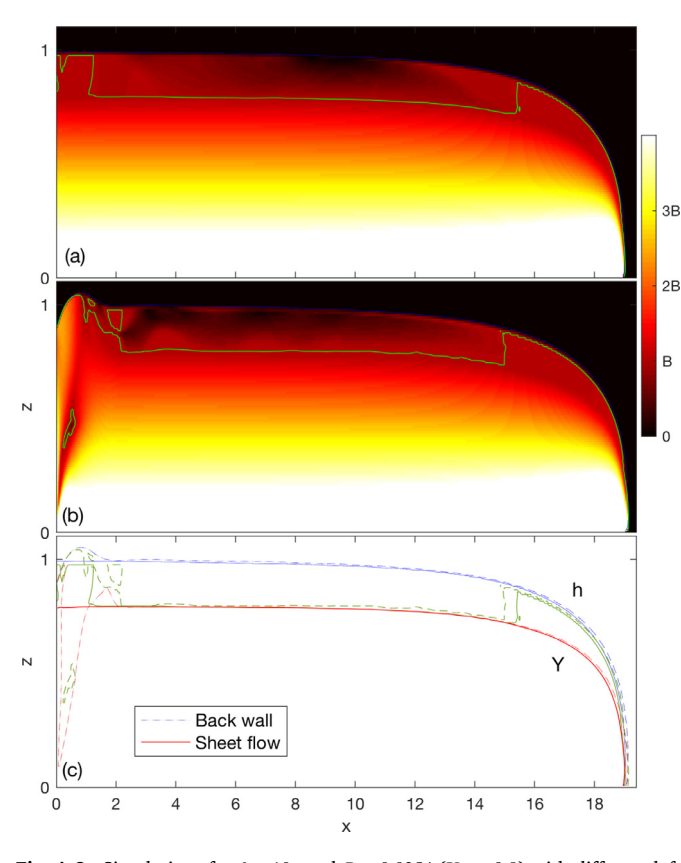


Fig. A.3. Simulations for $\theta=10^\circ$ and B=0.0354 ($Y_\infty=0.8$) with different left-hand boundary conditions: (a) $(u,w)=(u_{sheet},0)$ and (b) (u,w)=(0,0). Shown is the second invariant τ_I as a density on the (x,z)-plane. The (true) yield surfaces are indicated by the solid (green) lines. The simulation in (a) corresponds to the truncated solution shown in Fig. 3. The profiles and the true and fake yield surfaces are compared in (c).

A3. The effect of the back wall

To gauge the effect of the back wall on the computations, Fig. A.3 compares two simulations with different boundary conditions imposed along x=0. In the first, the velocity field corresponding to the uniform sheet flow is imposed (so $(u,w)=(u_{sheet},0))$; for the second, we impose a no-slip condition, u=w=0 The figure displays the stress invariant τ_I and plug regions; the solutions are much the same except within a region near the back wall in which flow adjustments arise due to the boundary condition there (and which changes the flow length slightly). In all our simulations, the extent of these flow adjustments was restricted to along-slope lengths of about 4H.

Appendix B. Improved lubrication solution

For Herschel-Bulkley fluid, the dimensionless system is

$$\begin{split} p_x &= \epsilon \sigma_x + \tau_z + S, & p_z &= -\epsilon \sigma_z + \epsilon^2 \tau_x - 1, \\ 0 &= \tau(x,h,t) + [p(x,h,t) - \epsilon \sigma(x,h,t)] h_x, \\ 0 &= p(x,h,t) + \epsilon \sigma(x,h,t) + O(\epsilon^2), \\ \begin{pmatrix} \sigma \\ \tau \end{pmatrix} &= \left(\dot{\gamma}^{n-1} + \frac{B}{\dot{\gamma}}\right) \begin{pmatrix} 2\epsilon u_x \\ u_z + \epsilon^2 w_x \end{pmatrix} \text{ for } 0 < z < Y, \\ B^2 &= \sigma^2 + \tau^2 \text{ for } Y < z < h, \\ \dot{\gamma} &= \sqrt{4\epsilon^2 u_x^2 + (u_z + \epsilon^2 w_x)^2}, \\ h_t &= -\left(\int_0^h u dz\right)_x \end{split}$$

In the fully yielded region, $u_z \sim O(1)$, $\sigma \sim O(\epsilon)$ and $\dot{\gamma} \sim O(1)$, and dropping the $O(\epsilon^2)$ terms then gives

$$p_z = -1 \qquad \text{and} \qquad p_x = \tau_z + S \tag{B.1}$$

Hence

$$p = h - z + P$$

$$\tau = (S - h_x - P_x)(Y - z) + B$$

$$Y = h + \frac{T - B}{S - h_x - P_x}$$
(B.2)

where P = P(x) and T = T(x), which further imply that

$$\tau = B + u_z^n,$$

$$u_z = (S - h_x - P_x)^{\frac{1}{n}} (Y - z)^{\frac{1}{n}},$$

$$u = \frac{n}{n+1} (S - h_x - P_x)^{\frac{1}{n}} \left[Y^{\frac{n+1}{n}} - (Y - z)^{\frac{n+1}{n}} \right] - u_b,$$
(B.3)

all to $O(\epsilon^2)$.

In the pseudo-plug, $u = u_p(x) - u_b + \epsilon u_1(x, z)$, and so

$$\dot{\gamma} = \epsilon \sqrt{4u_{px}^2 + u_{1z}^2 + O(\epsilon)} = \epsilon \Gamma.$$

Hence.

$$\begin{pmatrix} \sigma \\ \tau \end{pmatrix} = \frac{B}{\Gamma} \begin{pmatrix} 2u_{px} \\ u_{1z} \end{pmatrix} + O(\epsilon^n), \tag{B.4}$$

if n < 1. Thus

$$\sigma = \sqrt{B^2 - \tau^2} + O(\epsilon^n) \tag{B.5}$$

Force balance over this region demands

$$p_x = S + \tau_z + \epsilon \sigma_x$$
 & $p_z + \epsilon \sigma_z = -1 + O(\epsilon^2)$, (B.6)

which, given the surface stress conditions, now provide

$$p = h - z - \epsilon \sigma + O(\epsilon^{2}),$$

$$\tau = (S - h_{x})(h - z) + 2\epsilon \left(\int_{z}^{h} \sigma dz\right)_{x} + O(\epsilon^{2}),$$
(B.7)

or, given (B.5),

$$\tau = (S - h_x)(h - z) + \frac{1}{2}\epsilon B^2 \left(\frac{2\theta + \sin 2\theta}{S - h_x}\right) + O(\epsilon^{n+1}),$$

where

$$\theta = \sin^{-1} \frac{(S - h_x)(h - z)}{B}.$$
(B.8)

Next we observe that $P \sim O(\epsilon^2)$, because p = h - z + P and $\sigma = O(\epsilon)$ in the fully sheared region, but $p = h - z - \epsilon \sigma + O(\epsilon^2)$ in the pseudoplug. The match of $\tau = (S - h_x)(h - z) + T$ in z < Y with

$$(S-h_x)(h-z) + 2\varepsilon \left(\int_z^h \sqrt{B^2 - \tau^2} dz\right)_x + O(\varepsilon^{n+1})$$

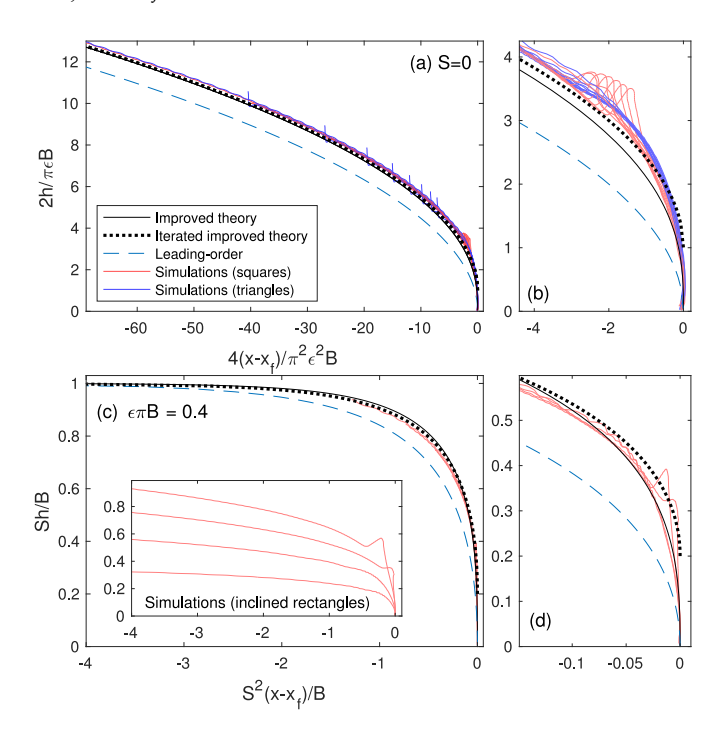


Fig. B.1. Slump profiles for (a)-(b) S=0 and (b)-(c) $S\neq 0$. For (a)-(b), scaled variables are plotted, which eliminates any free parameters; in (c)-(d) the profiles are shown for $\frac{1}{2}\epsilon\pi B=0.2$. The dark solid lines show the solutions to (38), whereas the dotted lines show the solutions to the iterated version in(40); the dashed lines show the leading-order approximation. In (a)–(b) the lighter (red and blue) lines show the results of a series of simulations from [22] with $\epsilon=1$, $B=0.02,\,0.03,\,\ldots,\,0.1$ and the flow fronts aligned. In (c)–(d) the lighter (red) lines show additional simulations of the slump of a rectangular block on an incline with $B=(0.1,0.2,0.3,0.4)/\pi$ and $\theta=5^\circ$; the inset shows the aligned, but unscaled profiles.

for z > Y, then demands that

$$T = 2\epsilon B \left(\int_{Y}^{h} \sqrt{1 - \frac{(S - h_{x})^{2}(h - z)^{2}}{B^{2}}} dz \right)_{x}$$
$$= \frac{1}{2} \epsilon \pi B^{2} \left(\frac{1}{S - h_{x}} \right)_{x}. \tag{B.9}$$

Now we match the velocity profile of the fully yielded region in (B.3) with that of the pseudo-plug $u=u_p-u_b+\epsilon u_1$, to find $u_1(x,Y,t)=0$ and

$$u_p = \frac{n}{n+1} (S - h_x)^{\frac{1}{n}} Y^{\frac{n+1}{n}}.$$

Finally we compute u_1 and the downslope flux: in the pseudo-plug,

$$\frac{u_{1z}}{2u_{px}} = \frac{\tau}{\sigma} = \frac{(S - h_x)(h - z)}{\sqrt{B^2 - (S - h_x)^2(h - z)^2}} + O(\epsilon),$$
(B.10)

and so, given that $(S - h_x)(h - Y) = B + O(\epsilon)$,

$$u_1 = 2u_{px}\frac{\sqrt{B^2-(S-h_x)^2(h-z)^2}}{S-h_x} + O(\epsilon).$$

The flux can then be computed as

$$\begin{split} \int_0^h u dz &= \int_0^Y u dz + \int_Y^h (u_p - u_b + \epsilon u_1) dz \\ &= u_p \Big(h - \frac{n}{2n+1} Y \Big) - u_b h + \frac{1}{2} \epsilon \pi B^2 \frac{u_{px}}{(S - h_x)^2} \end{split}$$

The equations of the improved model quoted in the main text now follow, on taking n = 1.

Appendix C. Improved slump profiles

Curiously, the improved model for slumped shapes on slopes given by (38) implies that

$$hh_x \sim -\frac{1}{2}\epsilon\pi B^2(h_x^{-1})_x$$
 or $h \sim [3\epsilon\pi B^2(x_f - x)]^{1/3}$,

for $x \to x_f$. This contrasts sharply with the solution of the iterated version of the model in (41) which has a finite depth at the edge. Evidently, the freedom afforded by the extra derivative allows us to reach the flow front with $h \to 0$ and $h_x \to -\infty$. This feature of the improved asymptotic theory was not appreciated in our earlier papers [22,23], where the simpler iterated version of the model was implemented.

Fig. B.1 compares the various asymptotic solutions, with or without a background slope. The two versions of the improved model differ by $O(\epsilon^2)$ away from the flow front; within a distance of $O(\epsilon^2)$ of $x = x_f$, however, the flow depths become $O(\epsilon)$ different, permitting the iterated version to terminate at finite depth. For comparison, Fig. B.1(a)-(b) also includes simulation data from figure 14 of [22] for dambreaks on a horizontal surface with either square or triangular initial conditions. The (red) corners visible in panel (b) are relics of square initial conditions, whereas the (blue) sharp spikes at the back evident in panel (a) are remnants from triangular initial conditions (in the scaled coordinates the slumps have different lengths). Further computations for the slump of a rectangular block on an incline (with unit height and an upstream back wall) are included in Fig. B.1(c)-(d). Both comparisons indicate that the two versions of the improved model outperform the leading-order theory away from the flow front. Near that steep feature, the smooth decline to zero thickness of the non-iterated model provides a slightly more satisfying comparison with simulations. However, the asymptotic theory is not valid at the flow front where the slope of the free surface diverges. Moreover, the surface in the numerical simulations eventually overturns to create multi-valued profiles with a finite elevation at the leading edge. Consequently, it is not clear which version of the improved model is superior; the iterated model (which we have employed previously, and continue to use in the main text) has the advantage of being the simpler.

References

- D. De Kee, R. Chhabra, M. Powley, S. Roy, Flow of viscoplastic fluids on an inclined plane: evaluation of yield stress, Chem. Eng. Comm. 96 (1) (1990) 229–239.
- [2] P. Coussot, S. Boyer, Determination of yield stress fluid behaviour from inclined plane test, Rheologica Acta 35(6) (1995) 534–543.
- [3] P. Coussot, S. Proust, Slow, unconfined spreading of a mudflow, J. Geophys. Res. Solid Earth 101 (B11) (1996) 25217–25229.
- [4] G. Hulme, The interpretation of lava flow morphology, Geophys. J. Int. 39 (2) (1974) 361–383.
- [5] P. Coussot, S. Proust, C. Ancey, Rheological interpretation of deposits of yield stress fluids, J. Non-Newton. Fluid Mech. 66 (1) (1996) 55–70.
- [6] D.I. Osmond, R.W. Griffiths, The static shape of yield strength fluids slowly emplaced on slopes, J. Geophys. Res.: Solid Earth 106 (B8) (2001) 16241–16250.
- [7] N. Dubash, N.J. Balmforth, A.C. Slim, S. Cochard, What is the final shape of a viscoplastic slump? J. Non-Newton. Fluid Mech. 158 (2009) 91–100.
- [8] S. Cochard, C. Ancey, Experimental investigation of the spreading of viscoplastic fluids on inclined planes, J. Non-Newton. Fluid Mech. 158 (2009) 73–84.
- [9] N. Andreini, G. Epely-Chauvin, C. Ancey, Internal dynamics of newtonian and viscoplastic fluid avalanches down a sloping bed. Phys. Fluids 24 (2012) 053101.
- [10] B. Bates, C. Ancey, The dam-break problem for eroding viscoplastic fluids, J. Non-Newton. Fluid Mech. 243 (2017) 64–78.
- [11] G. Chambon, A. Ghemmour, D. Laigle, Gravity-driven surges of a viscoplastic fluid: an experimental study, J. Non-Newton. Fluid Mech. 158 (2009) 54–62.
- [12] G. Chambon, A. Ghemmour, M. Naaim, Experimental investigation of viscoplastic free-surface flows in a steady uniform regime, J. Fluid Mech. 754 (2014) 332–364.
- [13] P. Freydier, G. Chambon, M. Naaim, Experimental characterization of velocity fields within the front of viscoplastic surges down an incline, J. Non-Newton. Fluid Mech. 240 (2017) 56–69.
- [14] K.F. Liu, C.C. Mei, Slow spreading of a sheet of Bingham fluid on an inclined plane, J. Fluid Mech. 207 (1989) 505–529.
- [15] N.J. Balmforth, R.V. Craster, R. Sassi, Shallow viscoplastic flow on an inclined plane, J. Fluid Mech. 470 (2002) 1–29.
- [16] N.J. Balmforth, R.V. Craster, A.C. Rust, R. Sassi, Viscoplastic flow over an inclined surface, J. Non-Newton. Fluid Mech. 139 (2006) 103–127.
- [17] I. Walton, S. Bittleston, The axial flow of a Bingham plastic in a narrow eccentric annulus, J. Fluid Mech. 222 (1991) 39–60.

- [18] N.J. Balmforth, Viscoplastic asymptotics and other techniques, Viscoplastic Fluids: From Theory to Application, CISM. Springer, 2018.
- [19] A. Putz, I. Frigaard, D.M. Martinez, The lubrication paradox and use of regularisation methods for lubrication flows, J. Non-Newton. Fluid Mech. 163 (2009) 62–77.
- [20] I. Frigaard, D. Ryan, Flow of a visco-plastic fluid in a channel of slowly varying width, J. Non-Newton. Fluid Mech. 123 (2004) 67–83.
- [21] J.-M. Piau, Axisymmetric slump and spreading of cohesive plastic soft materials: a yield stress measurement by consisto-rheometry, J. Rheol. 49 (6) (2005) 1253–1276.
- [22] Y. Liu, N.J. Balmforth, S. Hormozi, D.R. Hewitt, Two dimensional viscoplastic dambreaks, J. Non-Newton. Fluid Mech. 238 (2016) 65–79.
- [23] Y. Liu, N. Balmforth, S. Hormozi, Axisymmetric viscoplastic dambreaks and the slump test, J. Non-Newton. Fluid Mech. 258 (2018) 45–57.
- [24] M. Fortin, R. Glowinski, Augmented Lagrangian Methods: Applications to the Numerical Solution of Boundary-Value Problems, North-Holland, 2006.
- [25] A. Wachs, Numerical simulation of steady Bingham flow through an eccentric annular cross-section by distributed lagrange multiplier/fictitious domain and augmented lagrangian methods, J. Non-Newtonian Fluid Mech. 142 (2007) 183-198.
- [26] S. Hormozi, K. Wielage-Burchard, I. Frigaard, Entry and start up effects in visco-plastically lubricated viscous shear flow in pipe, J. Fluid Mech. 673 (2011) 432–467.

 [27] N. Balmforth, J. Liu, Roll waves in mud, J. Fluid Mech. 519 (2004) 33–54.
- [28] M. Renardy, Y. Renardy, J. Li, Numerical simulation of moving contact line problems using a volume-of-fluid method, J. Comp. Phys. 171 (2001) 243–263.